Northumbria Research Link

Northumbria University NEWCASTLE

UniversityLibrary

Article

Modification of Cantor High Entropy Alloy by the Addition of Mo and Nb: Microstructure Evaluation, Nanoindentation-Based Mechanical Properties, and Sliding Wear Response Assessment

Alexandros E. Karantzalis [1], **Anthoula Poulia** [2], **Spyros Kamnis** [3], **Athanasios Sfikas** [4], **Anastasios Fotsis** [1] **and Emmanuel Georgatis** [1,*]

[1] Department Materials Science and Engineering, University of Ioannina, 45110 Ioannina, Greece; akarantz@uoi.gr (A.E.K.); tasosfotsis13@gmail.com (A.F.)
[2] Department of Physics, University of Oslo, 0371 Oslo, Norway; anthoula.poulia@smn.uio.no
[3] Castolin Eutectic-Monitor Coatings Ltd., Newcastle upon Tyne NE29 8SE, UK; spyros@monitorcoatings.com
[4] Faculty of Engineering and Environment, Northumbria University, Newcastle upon Tyne NE1 8ST, UK; athanasios.sfikas@northumbria.ac.uk
[*] Correspondence: mgeorgat@uoi.gr

Abstract: The classic Cantor (FeCoCrMnNi) isoatomic high entropy alloy was modified by separate additions of Mo and Nb in an effort to optimize its mechanical properties and sliding wear response. It was found that the introduction of Mo and Nb modified the single phase FCC solid solution structure of the original alloy and led to the formation of new phases such as the BCC solid solution, σ-phase, and Laves, along with the possible existence of intermetallic phases. The overall phase formation sequence was approached by parametric model assessment and solidification considerations. Nanoindentation-based mechanical property evaluation showed that due to the introduction of Mo and Nb; the modulus of elasticity and microhardness were increased. Creep nanoindentation assessment revealed the beneficial action of Mo and Nb in increasing the creep resistance based on the stress sensitivity exponent, strain rate sensitivity, and critical volume for the dislocation nucleation considerations. The power law and power law breakdown were identified as the main creep deformation mechanisms. Finally, the sliding wear response was increased by the addition of Mo and Nb with this behavior obeying Archard's law. A correlation between microstructure, wear track morphologies, and debris characteristics was also attempted.

Keywords: high entropy alloys; microstructure; alloying; nanoindentation; creep; tribology

1. Introduction

Traditional alloy design routes focus on the mixture of one or two principal elements and the addition of minority elements in lower atomic ratios to form a final system possessing the optimum performance criteria. Up to now, following this route has led to the well-known families of steels, aluminum, titanium, and nickel alloys, which have offered a vast research area of exploration. Nonetheless, there still remains a space for the development of new alloys, characterized by improved properties in targeted application fields.

A novel approach to alloy design strategies was first established in 2004 by the pioneering work of Cantor et al. [1] and Yeh et al. [2], who simultaneously proposed the concept of high entropy alloys (HEAs). These systems were originally introduced as concentrated solid solutions of multiple principal elements in equal or near-equal concentrations of 5–35 at.%. Although HEAs were initially designed to benefit from single-phase stabilization [3], single-phase HEAs turned out to be not that common or easy to produce, and of those that do exist, only a few display an effective combination of high strength, ductility, and toughness [4]. The entropic factor is therefore inadequate by itself to maintain the initial phases of HEAs, so other thermodynamic and geometric parameters seem to

additionally influence the diverse phase structures of these systems [5]. Thus, an option of investigating systems consisting of two or more phases has opened up an unexplored region in the center of the compositional-phase space, giving birth to a wider improvement in the properties [6–8].

Among the many HEAs studied thus far, the first proposed alloy was the equiatomic FeCoCrMnNi system, also known as the Cantor alloy [1], which was defined as one of the first HEA systems with a FCC single-phase structure. Several properties of this system have been studied in recent years including the alloy's mechanical behavior in terms of the hardness [9–11], the compression properties [12,13], the tensile properties [14,15], the fracture toughness [16,17], and the nanoindentation behavior [18–33] at different temperatures.

The exceptional characteristics of the Cantor alloy have promoted this system as a strong candidate over other HEAs, however, engineering applications of the alloy are still severely constrained by its low strength values [34]. To overcome this drawback, the addition of extra elements to the phase structure of the Cantor alloy has been suggested as a way out to alter both its microstructure and properties.

There have been many studies on the composition regulation of the Cantor alloy. For instance, the addition of Al can affect the phase formation and microstructural evolution by a transition from the FCC phase to (Al, Ni, Fe)-rich B2 phase precipitates in the matrix when increasing the Al content [35]. Mo is beneficial to the formation of a sigma phase in the Cantor alloy [36], while the addition of Ti affects the grain size of the matrix, the precipitated phase, and its volume fraction [37]. Nb promotes the formation of the ordered Laves phase [38], while when Si is added to the alloy, the nanoscale structure is precipitated [39].

The effect of alloying on the mechanical properties has also been widely analyzed by highlighting different strengthening effects such as solid-solution strengthening, second-phase strengthening, and fine-grain strengthening when adding Al, Ti, or other elements such as Sn, Zr, or Cu to the FeCoCrMnNi core [40–42]. In particular, the addition of Al sharply increases the strength of the Cantor alloy, but its ductility is decreased [35]. Mo increases the compression resistance yield strength [36], while similarly, the compressive yield strength and Vickers hardness also increase when adding Nb [38]. Ti significantly improves the ductility and strength of the FeCoCrMnNi HEA [37] while with the addition of Zr and Cr, the yield strength of the Cantor alloy continues to increase, but its ductility tends to decrease [43]. Furthermore, to date, only a few studies have been conducted to comprehensively identify the creep mechanism of the Cantor alloy [44], but nanoindentation results on modified Cantor systems are hard to find in the literature.

Due to the high hardness and apparent thermal stability of the mechanical properties, the Cantor alloy possesses one of the interesting potential applications for HEAs, that of the wear resistance [45]. Nevertheless, there has been limited work on the wear behavior of this system over typical operating temperatures [46] and a complete lack of experimental studies on the modified Cantor alloy compositions.

Therefore, the basic motivation of this work is to fill in the literature gaps regarding Cantor modified alloys by studying the role of the addition of Mo and Nb at relatively small percentages (targeted 8 at.%) and a parallel slight increase in the Cr content (targeted 24 at.%). The deliberate control of primary and secondary hard phase (BCC, σ-phases, Laves) formation and its correlation with the mechanical (modulus of elasticity, hardness, creep resistance) and wear properties was also pursued.

The second technical novelty in the present effort deals with the way that the nanoindentation creep tests were performed on the modified Cantor compositions. The usual adopted approach is to alter the applied indentation load and the preset load to measure for different time intervals of the indentation creep. This approach gives different indentation depths for different materials (i.e., different material volume underneath the indenter that is affected and responds during the creep stage) [22]. In the present effort, the pre-creep depth was set constant (1000 nm), which practically means that all the tested alloys started on the same basis of pre-deformed status and as such, their creep response was directly comparable.

2. Materials and Methods

The examined systems were produced by mixing the constituent elements, which were in the form of powders with more than 99.5% purity. The mixtures (around 8 g in total) were formed in the shape of cylindrical pellets (14 mm diameter) using a hydraulic press (200 bar applied pressure, University of Ioannina, Ioannina, Greece), and the pellets were melted in a non-consumable electrode arc melting furnace (University of Ioannina, Ioannina, Greece), under a W non-consumable electrode and 120 A current, which established a temperature at the core of the arc around 2500 °C. Ti getter was used, and an argon atmosphere was established in order to prevent the oxidation phenomena. The melting process was performed on a water-cooled copper mold. The samples were flipped and re-melted five times, under the same conditions, to ensure homogeneity in the elements' distribution. This re-melting process is a common practice adopted in many research efforts dealing with HEAs. The samples produced after the melting process were in the form of meniscus with a diameter of around 10 mm at the base. These samples were subjected to mounting followed by the standard metallographic preparation procedure. This form of mounted samples was used in all the characterization procedures adopted in the present effort.

The microstructural features were assessed by the use of a scanning electron microscope (SEM) (JEOL 6510 LV, JEOL Ltd., Akishima, Tokyo, Japan) equipped with backscattered electron (BSE) and energy dispersive spectroscopy (EDS, Oxford Instruments Ltd. Abingdon, Oxfordshire, UK) detectors along with X-ray diffraction analysis (XRD) using an X-ray diffractometer (Bruker, D8 Advance, Bruker Ltd., Billerica, MA, USA) with Cu K$_\alpha$ radiation, ranging from 2θ = 10–120° and a scanning rate of 0.01°/s.

The dynamic indentation tests were performed using a Shimadzu DUH-211S nanoindenter (Shimadzu Ltd., Kyoto, Japan) with a standard Berkovich diamond tip at room temperature. Initial machine calibration was conducted on a fused silica standard to ensure the validity of the testing data. To remove the thermal effect, thermal drift was maintained at 0.05 nm s^{-1} during each test. The load holding time was settled at 20 s, during the creep stage. The indentation depth was set to 1000 nm and the loading speed was 13.324 mN/s. Average values and standard deviation were calculated based on at least 10 trials for each specimen.

Wear analysis was performed using a ball-on-disk tribometer (CSM Instruments, Peseux, Switzerland). The tests were performed under 2 N of applied load and 10 cm/s linear speed. A 100Cr6 steel ball with a 6 mm diameter was used as the counter-body. The overall sliding distance was set to 2000 m. Specimens were acetone cleaned and weighted before testing. Test runs were interrupted every 200 m and the specimens were re-weighted. Debris was collected after every 200 m interval. All corrections were mixed and the final mixture was examined by SEM-EDS. At least three runs were performed for each alloy system.

3. Results and Discussion

3.1. Microstructure Assessment

3.1.1. XRD Analysis

Figure 1 presents the XRD analysis examined in the present effort. As far as the plain Cantor alloy is concerned, it can be observed that it practically consisted of a single-phase solid solution of the FCC crystal structure. This microstructural observation is in agreement with both the other experimental efforts and the initial effort of Cantor [1,2] to design a single-phase multiple element (high entropy) alloy.
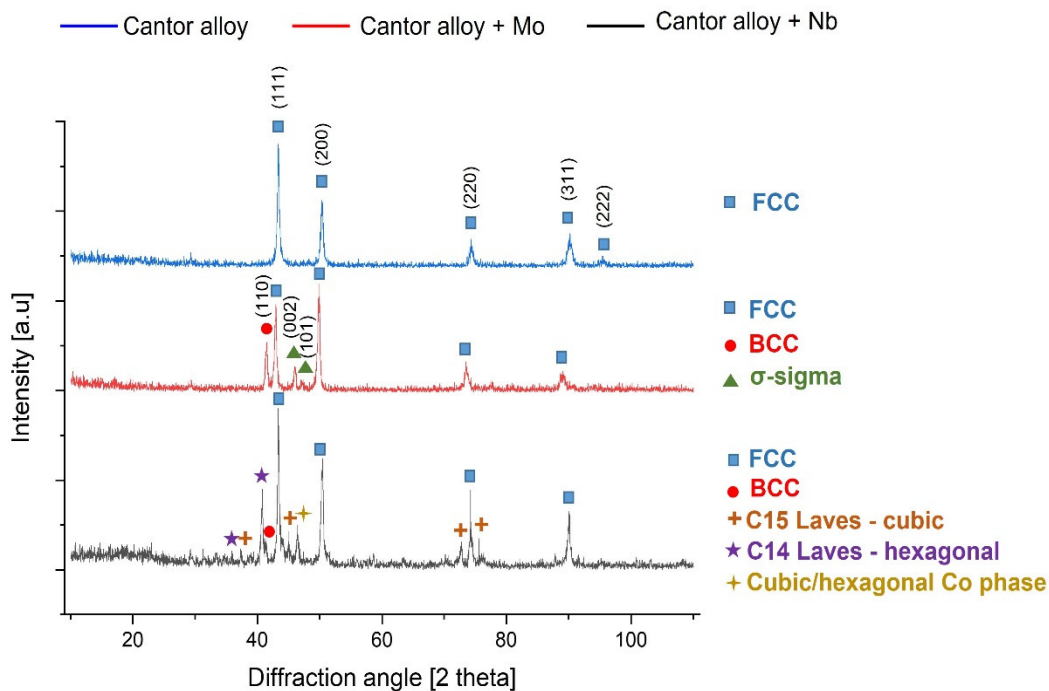
Figure 1. XRD diffractograms of the produced systems including the plain Cantor alloy showing a single FCC phase, the Mo modified system showing the presence of the FCC, BCC, and σ-sigma phases, and the Nb modified alloy showing a major FCC phase, possibly BCC, C14, and C15 Laves and possible cubic/hexagonal Co-based phases.

Regarding the XRD findings of the Mo modified alloy, it can be observed that the alloy mainly consisted of an FCC phase, followed by the formation of a BCC solid solution. The sigma, σ, phase was also identified. Some small intensity peaks were difficult to define by XRD, however, those located at the left part of the diagram can be associated with the presence of oxide phases formed during the manufacturing stage, whereas the other small peaks can be associated with the presence of other intermetallic phases such as the μ phase. In general, the analysis is in agreement with the work of Shun et al. [47], with the presence of BCC phase, however, not being reported in their effort. It should be noticed, nevertheless, that in their work, the amount of Cr was significantly lower compared to the one adopted in the present effort.

In the XRD analysis of the Nb modified system, the phase identification was somehow more complicated. It can be observed that apart from the major FCC phase, a possible BCC phase, Laves, and other possible intermetallic phases can also be present. He et al. [48] also reported the presence of Laves in their effort, along with a major FCC solid solution.

These experimental findings independently cannot support a solidification sequence for the different systems, yet in conjunction with the microstructural analysis described in the following paragraph, will assist in the formulation of a solidification mechanism.

3.1.2. Microstructural Analysis and Parametric Model Assessment

Figure 2a–c presents the microstructure of the produced systems after SEM examination and Figure 3a–c depicts the elemental EDS mapping analysis by showing the panoramic element distribution in each case along with the overall actual system compositions. The Cantor alloy (Figures 2a and 3a), as expected, consisted of a single phase with practically no phase segregation, a uniform elemental distribution, and an actual composition not differing significantly from the targeted one.

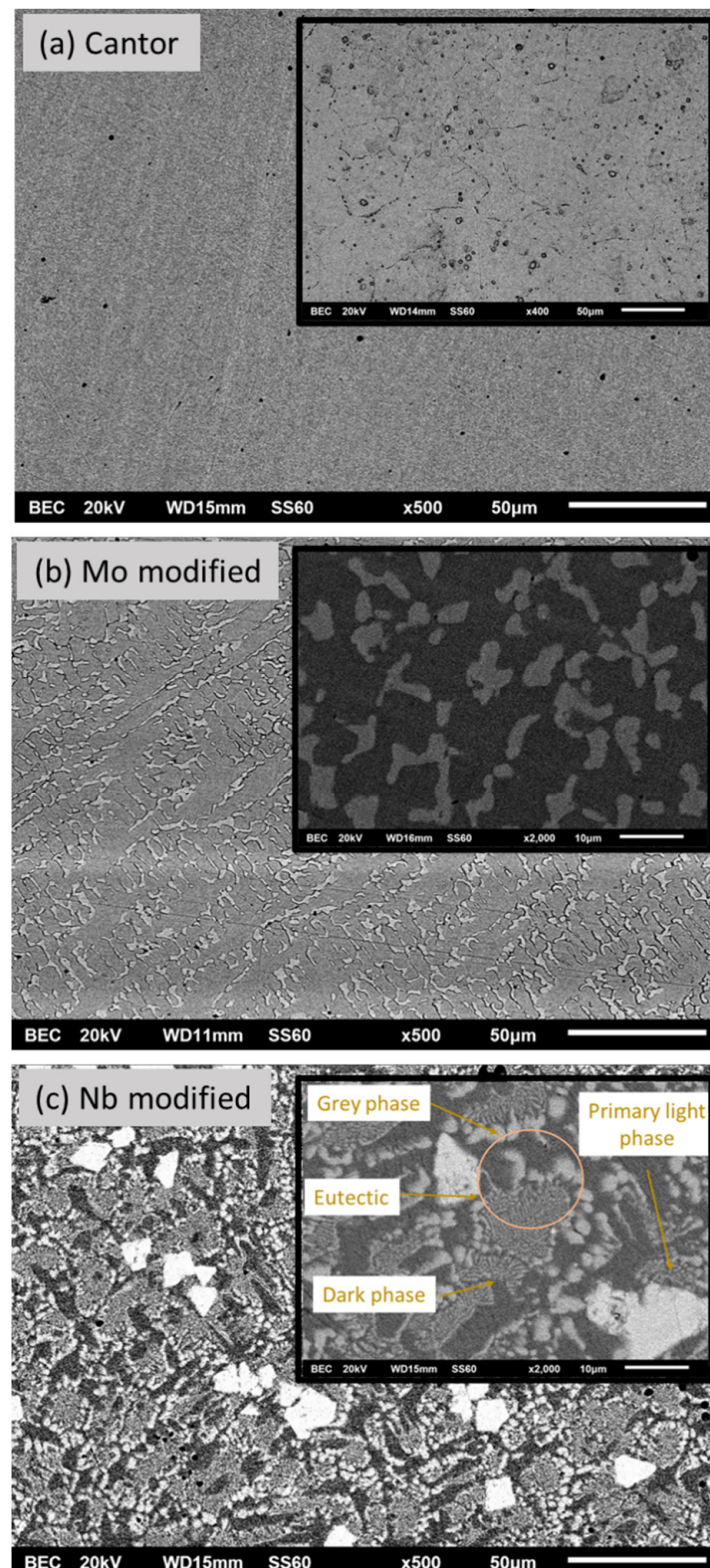**Figure 2.** SEM images of the different system microstructures. (**a**) The plain Cantor alloy showing one phase and no segregation. Some porosity is present; (**b**) the Mo modified system showing the existence of two segregated phases: primary light and secondary dark; and (**c**) the Nb modified system showing the presence of primary light, grey, and dark phases. The eutectic microconstituent is evident.

Figure 3. EDS mapping of the produced alloys. (**a**) The Cantor alloy showing uniform element distribution; (**b**) the Mo modified alloy showing also uniform element distribution; and (**c**) the Nb modified system showing preferential segregation of Nb within the primary light phase.

The microstructure of the Mo modified system is presented in Figures 2b and 3b, respectively. It can be observed that it consists of two phases: a primary white/bright phase and a dark phase. The elemental mapping (Figure 3b) analysis did not show a clear elemental preferential distribution and, thus, a point analysis was necessary (Figure 4a). The actual composition of the system resulting from the mapping analysis also did not differ from the one initially designed. The EDS point analysis (Figure 4a) showed that the primary phase was enriched in Mo and Cr with significant amounts of the other elements being dissolved within it, whereas the dark phase was enriched in the other, but the Mo and Cr elements, in general. Karantzalis and co-workers [49–51] extensively reported on the combination of Mo and Cr to form BCC phases in other systems where Mo and Cr were present, and this is a strong reason why in the present effort, the authors claim that the primary phase is a BCC phase rather than a σ-sigma phase, as proposed by Shun et al. [47].

Figures 2c and 3c show the microstructural characteristics of the Nb modified system. Clearly, the morphological features were more complicated in this case. It can be observed that the system consists of (a) a primary light/bright phase; (b) a eutectic microconstituent consisting of a dark and a grey phase; (c) a dark phase both present in the eutectic area and surrounding the primary light phase; and (d) a gray phase that seems to be initiated within the eutectic region and gradually coarsened toward the last areas of solidification.

Mo modified	EDS point composition (at.%) ●	EDS point composition (at.%) ▲
Cr	29.30 ± 2	25.10 ± 3
Mn	12.90 ± 3	14.10 ± 2
Fe	16.00 ± 1	19.00 ± 2
Co	16.50 ± 1	13.30 ± 1
Ni	11.80 ± 2	17.40 ± 2
Mo	13.50 ± 3	6.10 ± 3

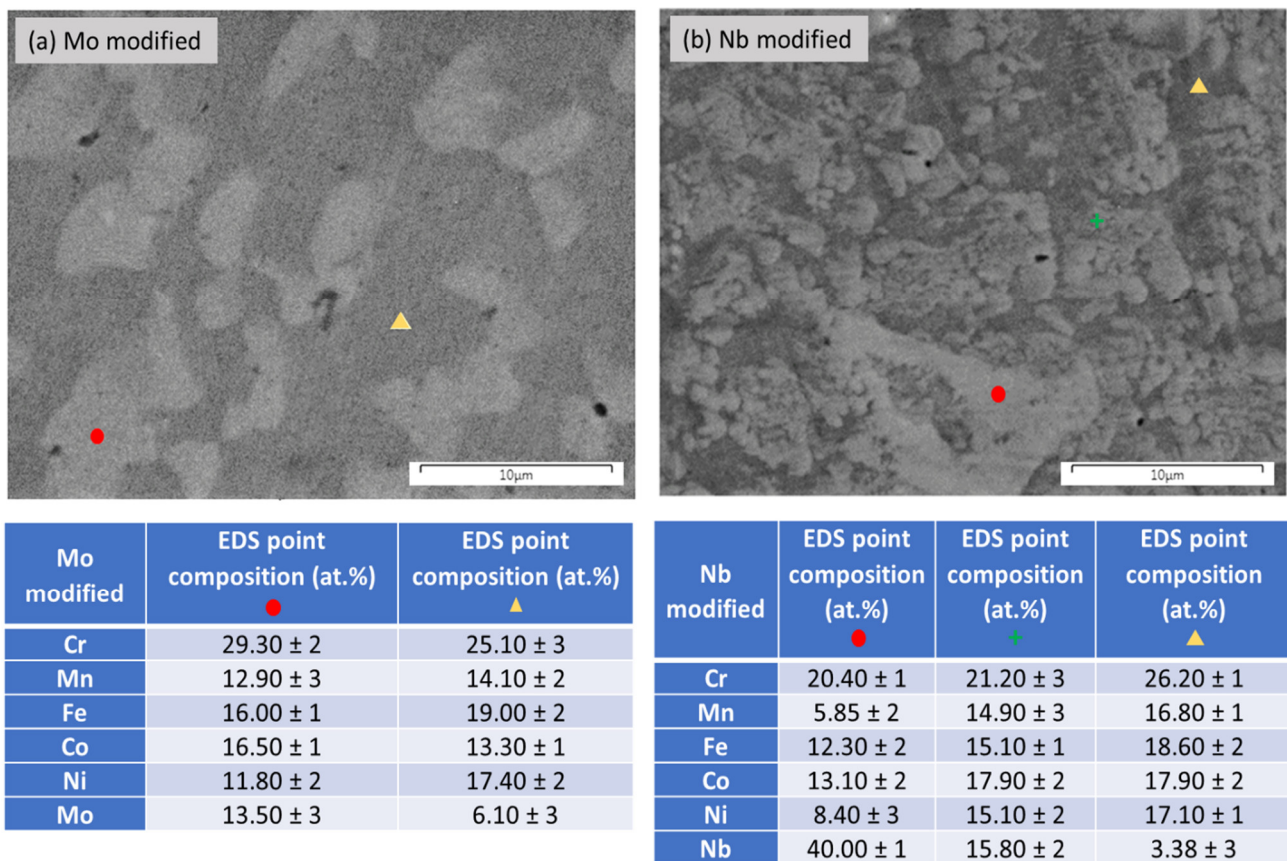| Nb modified	EDS point composition (at.%) ●	EDS point composition (at.%) +	EDS point composition (at.%) ▲
Cr	20.40 ± 1	21.20 ± 3	26.20 ± 1
Mn	5.85 ± 2	14.90 ± 3	16.80 ± 1
Fe	12.30 ± 2	15.10 ± 1	18.60 ± 2
Co	13.10 ± 2	17.90 ± 2	17.90 ± 2
Ni	8.40 ± 3	15.10 ± 2	17.10 ± 1
Nb	40.00 ± 1	15.80 ± 2	3.38 ± 3

Figure 4. EDS point analysis. (**a**) The Mo modified alloy with the primary light phase being enriched in Mo and (**b**) the Nb modified alloy showing the primary light phase being rich in Nb and the dark phase almost depleted in Nb.

EDS point analysis was also conducted (Figure 4b) to verify the compositions of these phases. The EDS mapping (Figure 4b) clearly showed a segregation of Nb within the primary light phase, while the actual composition was very close to the one initially targeted. The point analysis of the involved phases revealed that: (a) The primary phase was rich in Nb and it is worth mentioning that the relative ratio of Nb-Cr was almost 2 to 1; (b) the grey phase showed an almost equiatomic composition with Cr being slightly increased; and (c) the main feature of the dark phase was that it is depleted in Nb.

The observations and the analysis by SEM-EDS and the data obtained by XRD will assist in the formulation of a potential solidification sequence. Nevertheless, prior to that, it was interesting to examine the contribution of the parametric models in predicting the possible phase segregation phenomena. Table 1 summarizes the overall compositions (nominal and actual), the composition of each individual phase, and the values of the basic parametric model parameters for both the overall and each individual phase composition. Table 2 also presents an enthalpy matrix of the calculated enthalpies of formation for the lowest energy structures of the binary compounds present in the three alloys.

In the case of the monolithic Cantor alloy, it could be observed that the Zhang et al. models [52] (namely atomic size difference (δ), enthalpy of mixing (ΔH_{mix}), and entropy of mixing (ΔS_{mix})) were fulfilled, with the involved parameters obtaining values that predicted a single solid solution phase for both the nominal and actual compositions ($-22 \leq \Delta H_{mix} \leq 7$ kJ/mol, $\delta \leq 8.5$, and $11 \leq \Delta S_{mix} \leq 19.5$ J/(K·mol)). Toward this direction, the model of Wang et al. [53] with the geometric factor γ, which takes into consideration the atomic size contribution and determines the solubility of multicomponent alloys, was also fulfilled and therefore a single phase was predicted.

Table 1. Nominal composition, actual overall composition, elemental compositions of the different phases, and the parametric prediction model values.

Composition at.%																
Phase \ Alloy	Cantor					Cantor + Mo						Cantor + Nb					
	Cr	Mn	Fe	Co	Ni	Cr	Mn	Fe	Co	Ni	Mo	Cr	Mn	Fe	Co	Ni	Nb
Nominal	20.0	20.0	20.0	20.0	20.0	24.8	16.8	16.8	16.8	16.8	8.0	24.8	16.8	16.8	16.8	16.8	8
Actual	20.1	19.2	20.5	20.8	19.4	24.7	15.3	17.5	17.8	16.8	7.9	24.6	15.7	17.0	16.4	16.4	9.1
Matrix						25.1	14.1	19.0	18.3	17.4	6.1						
Primary phase						29.3	12.9	16.0	16.5	11.8	13.5						
Light phase												20.4	5.9	12.3	13.1	8.4	40
Gray phase												21.2	14.9	15.1	17.9	15.1	15.8
Dark phase												26.2	16.8	18.6	17.9	17.1	3.38

Parametric Models											
Alloy	Cantor		Cantor + Mo				Cantor + Nb				
Model \ Phase	Nominal	Actual	Nominal	Actual	Matrix	Primary	Nominal	Actual	Light Phase	Gray Phase	Dark Phase
δ	3.27	3.22	3.65	3.58	3.40	3.79	4.58	4.69	6.60	5.40	3.83
ΔS_{mix} [J/K mol]	13.38	13.38	14.52	14.51	14.33	14.44	14.52	14.58	13.20	14.82	14.03
ΔH_{mix} [kJ/mol]	−4.16	−4.09	−3.96	−3.99	−4.01	−3.51	−8.06	−8.56	−16.44	−11.43	−5.80
ΔG	−31.76	−31.73	−35.59	−35.62	−35.05	−35.15	−39.52	−40.33	−49.33	−44.53	−35.65
VEC	8	8	7.68	7.71	7.76	7.41	7.60	7.58	6.63	7.43	7.73
Ω	5.76	5.86	6.99	6.94	6.76	8.19	3.41	3.25	1.78	2.54	4.49
γ	1.096	1.096	1.107	1.107	1.107	1.107	1.167	1.167	1.164	1.166	1.168
T_m [K]	1790	1793	1905	1908	1892	1994	1893	1906	2218	1960	1854
$\Delta H_{IM}/\Delta H_{mix}$	1.66	1.65	2.35	2.29	2.13	2.75	2.75	2.83	3.60	2.99	2.36
k_1^{cr}	3.30	3.34	3.80	3.78	3.71	4.28	2.36	2.29	1.71	2.02	2.79

Table 2. Enthalpy matrix. Calculated enthalpies of formation of the binary compounds present in the three examined alloys.

Element \ Element	Cr	Mn	Fe	Co	Ni	Mo	Nb
Cr	0	−110	−8	5	−30	42	−47
Mn	−110	0	9	−19	−115	−136	−153
Fe	−8	9	0	−60	−97	−484	−2505
Co	5	−19	−60	0	−21	−52	−150
Ni	−30	−115	−97	−21	0	−100	−316
Mo	42	−136	−484	−52	−100	0	0
Nb	−47	−153	−2505	−150	−316	0	

Energy scale (meV/atom)

−500 −100 −300 −200 −100 −10   10   100 200 300

The valance electron concentration (*VEC*) criterion proposed by Guo et al. [54] also predicted the formation of a single FCC phase, which was indeed the case in the present effort. The Ω ($\Omega = T_m \Delta S_{mix}/|\Delta H_{mix}|$) and δ parameters also possessed values that fulfilled the Yang and Zhang [55] model for the formation of a single solid solution phase, while a similar situation was found for the model of Senkov et al. [56], where the k_1^{cr} parameter was higher than the $\Delta H_{IM}/\Delta H_{mix}$ ratio, thus predicting a single solid solution. Finally, the Troparevsky model [57] was also fulfilled for the Cantor composition, since all calculated enthalpies of formation (ΔH_f) for the binary components escalated inside the recommended boundaries (color legend of the energy scale is underneath the enthalpy matrix) for the formation of a simple phase solid solution ($-137 < \Delta H_f < 37$ meV/mol) regarding a 5-

component alloy. It can be said thus, that in the case of the Cantor alloy, all the parametric models successfully predicted the formation of one single phase alloy.

In the case of the Mo modified alloy, especially as far as the nominal and the actual compositions are concerned, it can be observed that all the parametric models were fulfilled with the exemption of the models proposed by Troparevsky et al. [57] and Guo et al. [54]. According to Troparevksy's model [57] it seems that the combination of Mo and Fe could provide phases with extremely low ΔH_f values (red color scale), which lay outside the proposed range for the formation of a simple phase solid solution. The *VEC* values in the case of Guo's model [54], although very close for the stability of a single FCC phase, were less than the proposed limit of 8. As such, concerns about a possible segregation were established, which were eventually verified by the actually obtained microstructure.

Similar to the previous case, observations could be made in the case of the Nb modified alloy. In this system, for both the nominal and the actual compositions, three models were not fulfilled. According to Troparevsky's model [57], Nb and Fe may form phases of very low ΔH_f values outside the stability range (red color scale). The *VEC* values were also less than 8, according to Guo's predictions [54], and finally, the model proposed by Senkov et al. [56] was also not fulfilled, since the $k_1{}^{cr}$ values for the nominal and the actual compositions were less than their relative $\Delta H_{IM}/\Delta H_{mix}$ ratios. The aforementioned divergences suggest possible phase segregation, as was the case observed in the actual microstructure.

The parametric model examination shows that, although not sufficient to predict which actual phases could be formed, it is indeed a useful tool, especially in the initial designing stages of new systems.

3.1.3. Possible Solidification Sequence

In the case of the monolithic Cantor alloy, simply upon cooling, a single phase FCC solid solution phase was formed.

For the Mo modified system, the following remarks can be made:

- At the initial stages of solidification, upon cooling, Mo is the element with the highest melting point and as such, drives the solidification process. By combining it with Cr, it forms the primary BCC solid solution phase, which also contains considerable amounts of the other elements being dissolved within it.
- Once the primary phase is formed, the last to solidify the liquid forms the FCC phase.
- Caution should be taken as potential σ-sigma phase formation may also take place, which is, however, difficult to be ascertained through SEM-EDS analysis.

In the case of the Nb modified alloy, the following points can be mentioned:

- Nb and Cr seem to control the initial stages of solidification. The primary light phase, according to the EDS analysis, is rich in Nb and Cr with their relative ratio of almost 2:1. Nevertheless, the overall actual composition of the alloy (Table 1) indicates Nb and Cr at a ratio of almost 1:2. It is thus obscure to expect the formation of a Nb rich phase in a system where Cr dominates. Nevertheless, the Cr-Nb phase diagram (Figure 5) [58] may enlighten this grey zone and assist in the solidification of the primary phase. According to the phase diagram, for the relative overall composition of the system where the ratio of Nb to Cr is 1:2, the Laves phase C14 of a cubic crystal structure and with a stoichiometry of Cr_2Nb can be formed. It was also interesting to note that from both sides of the Laves phases, a gap in the BCC structure also existed, the presence of which is very crucial. Based on these observations, it can be proposed that the solidification of the primary phase commences with the formation of C14 Laves. Once the C14 phase is formed, it locally depletes the remaining melt form Cr, and as such, it may shift the composition to the right area of the Laves region and upon temperature decrease, the system can be located within the BCC phase area where a BCC phase rich in Nb can be formed. This scenario of the formation of C14 and BCC phases is in agreement with the data presented in the XRD analysis.

- Once the primary phase is formed, the remaining melt seems to follow the postulates of He et al. [48] and behaves as a eutectic system with FCC and C15 Laves as the involved phases. As the temperature decreased, the established undercooling conditions led to the formation of the first eutectic structure, which was fine. As the development of the eutectic structure proceeded due to recalesence and the related heat release, the kinetics of the eutectic development became slower and as such, the eutectic gradually obtained a coarser structure. At the very last stages of the eutectic solidification, the kinetics were significantly retarded and the characteristic lamellae morphology vanished, giving space to more independent decoupling growth of the involved phases. Similar observations can be found in other works by Karantzalis and co-workers [49–51].
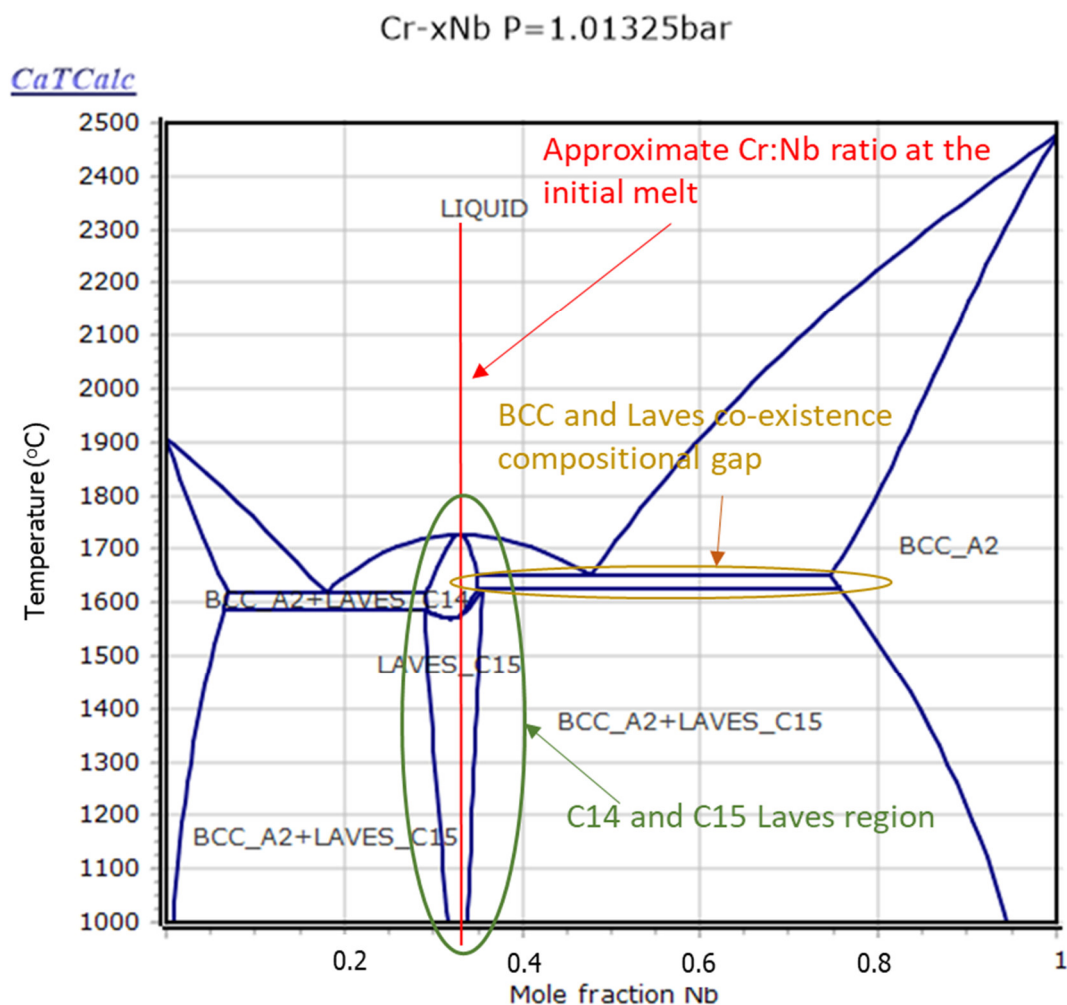

Figure 5. Modified Cr-Nb phase diagram after [58]. The red line shows the relative ratio of the Cr:Nb in the actual composition of the Nb modified alloy. The presence of the compositional gap (yellowish area) explains the presence of the BCC and Laves phases.

3.2. Nanoindentation Based Mechanical Property Assessment

Basic Mechanical Property Calculation

Table 3 summarizes the values obtained by the nano-indentation testing for the standard mechanical properties, namely E_{it} (indentation modulus of elasticity), n_{it} (absorbed energy in the elastic region/overall absorbed energy), and *HV* (hardness). The values were obtained at the preset depth of 1000 nm and for a single load–unload cycle (no holding time) at a preset loading speed of 13.324 mN/s. Ten repetitions were conducted for each alloy system. It has been mentioned that the calculation of these properties are based on

the approach of Oliver–Pharr for non-indentation testing [20] and are provided directly from the nano-indenter software.

Table 3. Values of the basic mechanical properties measured by nanoindentation.

System	E_{it} (GPa)	HV	n_{it} (%)
Cantor	200 ± 7	271 ± 10	11.7 ± 2
Mo modified	213 ± 10	468 ± 30	18.6 ± 4
Nb modified	230 ± 10	490 ± 35	22.0 ± 7

Based on the values of Table 3, the following points can be addressed:

(1) Modulus of elasticity (E_{it}): It can be seen that there was a slight increase in E_{it} after the modification of the basic Cantor alloy by Mo and Nb. More specifically, the E_{it} values were 200 ± 7, 213 ± 10, and 230 ± 10 for the plain Cantor alloy, the Mo modified system, and the Nb modified system, respectively. A possible explanation for this even slight increase can be associated with the microstructure and the involved phases in each case. By recalling the observations in the microstructure session, the plain Cantor alloy is a single-phase FCC solid solution with a lattice distortion δ value of 3.26, as calculated by the various parametric models. Lattice distortion mirrors the stress field experienced within the lattice and as such, can be associated with the modulus of elasticity measured in each case. The modification of the basic alloy by the addition of Mo led to phase segregation and the presence of two main phases. As shown in Table 3, the phases that were formed in this system had δ values of 3.80 (primary phase) and 3.40 (secondary phase or matrix). The nano-indentation tests were randomly performed on the specimen surface and as such, the calculated values were the average of the contribution of both segregated phases. Both the δ values of these phases were slightly higher than that of the plain Cantor alloy and as such, their overall contribution provided a δ value higher than the monolithic alloy, resulting in a slightly higher E_{it} value (213 GPa). The same approach also stands for the Nb modified alloy. The situation was even more intensive as the microstructure consisted of various segregated phases with their δ values ranging from 3.83 up to 6.60. These values were even higher and as such, their overall contribution resulted in an even higher average δ value, which was finally depicted by an even higher E_{it} value (230 GPa). Similar observations can also be found in other experimental efforts [29,59,60].

(2) Hardness *HV*: Table 3 clearly shows that the modification of the monolithic Cantor alloy by Mo and Nb led to a significant alteration in the initial hardness *HV*. More specifically, the *HV* values were found to be 271 ± 10, 468 ± 30, and 490 ± 35. It can also be observed that the hardness alterations were by far more significant than the modulus E_{it}. Since hardness is considered to be the resistance of the system to plastic deformation, this means that the modification by Mo and Nb caused a significant negative effect on the dislocation mobility and plastic deformation, leading to a significant increase in the hardness values. The reasons for such an increase can be as follows: (a) Lattice distortion: The higher the lattice distortion, the higher the stress field within the lattice, and the more restricted the dislocation movement. (b) Multiple phases of different crystal structure: The Cantor alloy is an FCC alloy whereas the Mo modified system, according to both the XRD and the SEM analyses, apart from FCC, also contained the BCC and σ phases, which by nature exhibit low dislocation mobility and lower plastic deformation. This trend becomes more severe in the case of the Nb modified system, where additionally to the previous, intermetallic phases may also being present. (c) Increase of phase and grain boundaries: By recalling the microstructures of the examined system, it was observed that from the simple one phase grains of the monolithic Cantor alloy, at least two segregated phases where observed in the case of the Mo modified alloy, whereas in the case of the Nb addition,

the microstructure became even more complicated with the presence of primary phases and eutectic morphologies. Thus, a sequence of the progressive development of more complicated microstructures associated with a progressive formation of more phase and grain boundaries was observed. This extensive boundary network also constitutes significant obstacles to the dislocation movement, and therefore to plastic deformation. All of these remarks are also in agreement with other research works [23,24].

(3) n_{it} ratio: The n_{it} ratio, by definition, follows the trend of the hardness values. Since the hardness is increased by the addition of Mo and Nb (i.e., the resistance in plastic deformation is accordingly increased), the energy absorbed in the elastic region is increased (i.e., the n_{it} ratio is altered in the same manner as the hardness).

3.3. Creep Assessment

3.3.1. Calculation Frame

For the necessary calculations to be conducted, the approaches of Karantzalis et al. [61,62], Zhang et al. [27], Ma et al. [24], and Wang et al. [63] were adopted, with some necessary modifications for simplicity reasons.

During a standard nanoindentation test with a Berkovitch indenter, the strain rate and hardness can be given by the following equations as functions of the indentation depth:

$$\dot{\varepsilon} = \frac{1}{h}\frac{dh}{dt} = \frac{\dot{h}}{h} \tag{1}$$

and

$$H = \frac{P}{24.5h^2} \tag{2}$$

where $\dot{\varepsilon}$ is the strain rate; H is the hardness; P is the applied load as the function of time; and h is the indentation depth as a function of time.

In the present effort, the creep stage started when the preset depth of roughly 1000 nm was reached. Once this preset depth was reached, the holding stage for 20 s at the reached load (P_{max}) took place. The net (pure) indentation depth due to creep can be calculated using the calculation methods of the already mentioned works [24,27,30,61,62] and is

$$h(t)_{creep} = at^p + kt \tag{3}$$

where t is the holding duration; and a, p, and k are the fitting parameters.

The overall indentation depth thus, will be:

$$h(total) = h_0 + at^p + kt \tag{4}$$

where h_0 is the indentation depth at the onset of the creep stage and is close to 1000 nm, which is the selected indentation depth.

According to Lin et al. [26] and Yu et al. [64], the indentation creep follows an empirical power law of the form

$$\dot{\varepsilon} = A\sigma^n \, exp\left(-\frac{Q}{RT}\right) \tag{5}$$

where A is a constant; n is the creep stress exponent; σ is the applied stress; and Q is the activation energy. Since all of the tests in the present effort were conducted at room temperature, the exponential factor of Equation (5) was considered to be constant and as such, Equation (5) can be rewritten as

$$\dot{\varepsilon} = \lambda\sigma^n. \tag{6}$$

By applying the logarithmic function on both sides of Equation (6), it becomes clear that

$$ln(\dot{\varepsilon}) = ln(\lambda) + n ln(\sigma) \tag{7}$$

Additionally, by applying the logarithmic function on both sides of Equation (1), we obtain

$$ln(\dot{\varepsilon}) = ln\left(\frac{1}{h}\frac{dh}{dt}\right) \tag{8}$$

Since Zhang et al. [27] and Wang et al. [63] proposed that

$$\sigma = kH \tag{9}$$

with k being a material constant, by plotting $ln(\dot{\varepsilon})$ (i.e., $ln\left(\frac{1}{h}\frac{dh}{dt}\right)$ with $ln(H)$), it is possible to calculate the stress exponent n and from this, the strain rate sensitivity m, as simply $m = 1/n$.

Figure 6a shows a typical example of the fitting curve along with the relevant fitting parameters and Figure 6b presents an example of the $ln\left(\frac{1}{h}\frac{dh}{dt}\right)$ vs. $ln(H)$ curve along with the linear fitting to calculate the stress exponent n (indicative creep curve for the plain Cantor alloy).
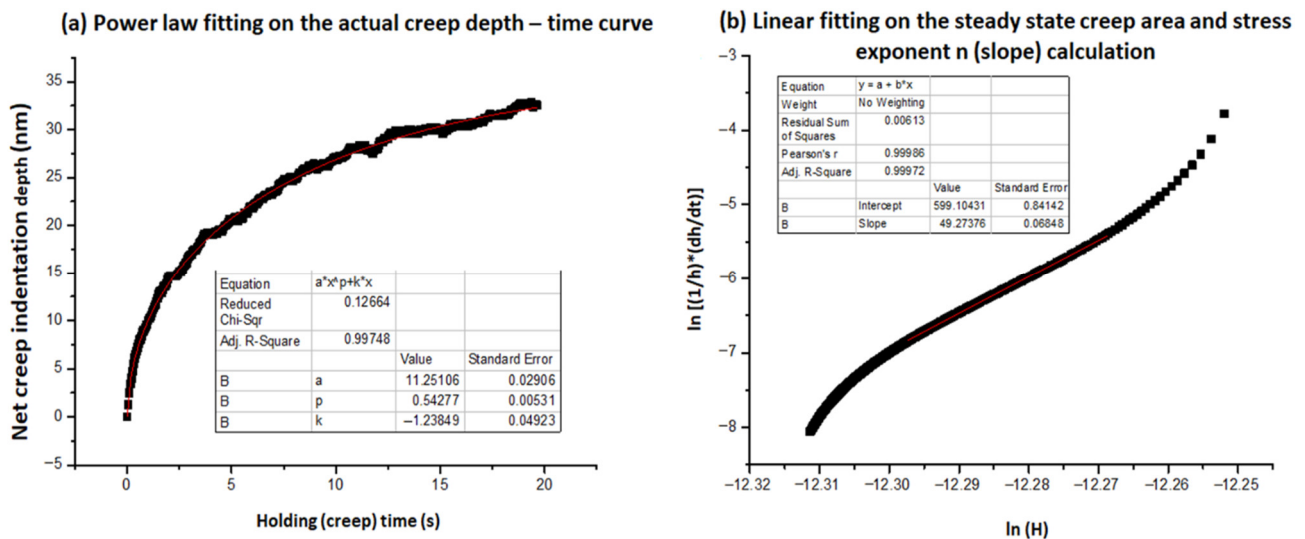

Figure 6. (**a**) Typical example of the fitting curve on the creep depth–time values along with the relevant fitting parameters and (**b**) an example of the $ln\left(\frac{1}{h}\frac{dh}{dt}\right)$ vs. $ln(H)$ curve along with the linear fitting to calculate the stress exponent n.

Once the stress exponent n and the strain rate sensitivity m are calculated, the critical volume for dislocation nucleation, V_{cr}, can also be calculated. According to Ma et al. [24] and Wang et al. [63],

$$V_{cr} = \frac{kT}{\tau_{max}m} \tag{10}$$

where k is the Boltzmann constant; T is the temperature in Kelvin degrees (298 K in the present effort); m is the strain rate sensitivity; and τ_{max} is the maximum shear stress applied during the creep stage. Following the approach of Wang et al. [63],

$$\tau_{max} = \frac{H_{max}}{3\sqrt{3}} \tag{11}$$

Accordingly,

$$H_{max} = \frac{P_{max}}{24.5 h_0^2} \qquad (12)$$

H_{max} is calculated using Equation (12) since the maximum load is experienced once the indenter has reached the preset for the creep indentation depth (1000 nm) and h_0 is always close to this value (~1000 nm).

3.3.2. Creep Results

Prior to any assessment of the actual creep stage during a nano-indentation test, it is important to examine the pre-creep loading stage. This pre-creep loading stage has been reported to be of high importance, since it is possible that creep phenomena and creep deformation could occur during this stage, which are drained out the net creep stage and do not allow for the system to express its net creep behavior during the actual creep stage [27].

Figure 7a shows the representative curves of the loading—prior to creep—stage for the examined systems in the present effort, where it can be observed that there was a lack of the characteristic "serration" morphology, which is usually an indication of creep phenomena during the loading stage [27]. This practically means that in the examined alloys, the initially present (from the production stage) dislocations and/or the dislocations generated during the loading stage did not show any marginal mobility upon a steady load that could account for even small creep deformation. Marginal creep deformation upon loading is usually experienced at low loading speeds [27], since the time for possible stress relaxation due to creep deformation is high. In the present effort, the adopted loading speed of 13.324 mN/s was high enough to prevent such phenomena from occurring.
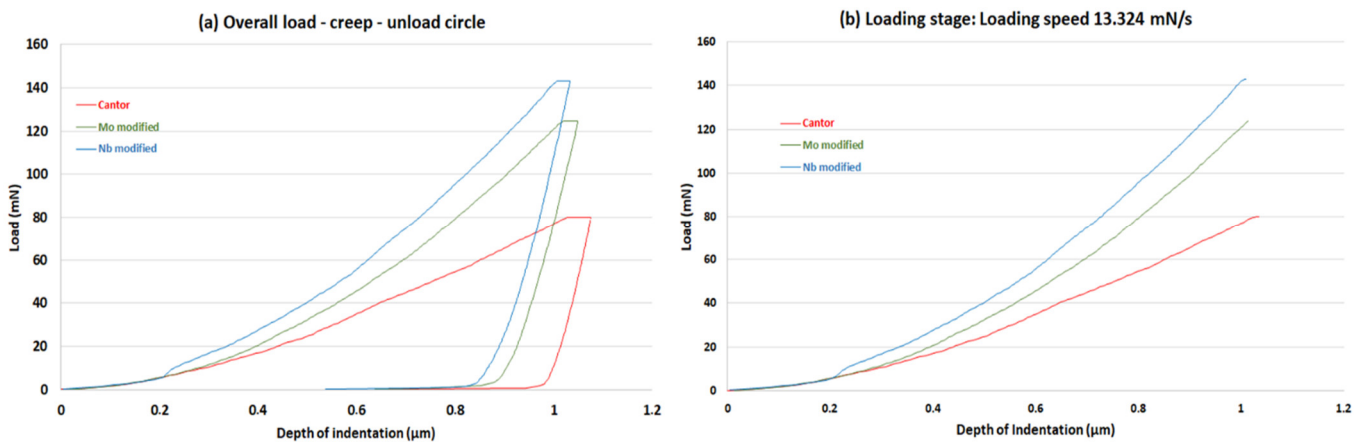

Figure 7. (a) Representative curves of the loading—prior to creep—stage for the examined systems. No significant evidence of "serrations" could be observed and **(b)** representative curves for the loading–creep stage–unload cycle of the examined systems. In order for the preset depth to be reached, the applied load increased from the plain monolithic Cantor alloy to the Mo modified and the Nb modified alloys.

Caution should be taken, however, in the case of the Nb modified system, where some more intensive, compared to the other systems, load–indentation depth fluctuations could be observed. By recalling the microstructure of this system, an extensive network of phase/grain boundaries was established due to the presence of multiple phases, especially the extent of the eutectic micro-constituent. Ma et al. [24] and Hu et al. [65] reported possible creep phenomena due to grain boundary sliding and migration, and even though this was not entirely the same case in the present effort, the authors do recognize that further experimentation is required in this direction.

Figure 7b shows the representative curves for the loading–creep stage–unload cycle of the examined systems. What is evident from these curves is that in order for the preset depth to be reached, the applied load increased as we moved from the plain monolithic Cantor alloy to the Mo modified and the Nb modified alloys. This trend was practically the same as the hardness of the systems and depicts the resistance each alloy showed toward plastic deformation.

Figure 8a presents the characteristics curves of the net creep indentation depth as a function of time for the different alloy systems. Clearly, the net Cantor alloy exhibited the higher creep depth values, followed by the Mo modified alloy, and the Nb alloy showed the lowest creep indentation depth. This is the first evidence that the Nb modified alloy showed a lower creep deformation (i.e., the higher creep resistance compared to the other two systems). This behavior is also supported by the data presented in Table 4. Figure 8b shows the characteristic $ln\left(\frac{1}{h}\frac{dh}{dt}\right)$ vs. $ln(H)$ curves of the systems, in order to calculate the n and m parameters.
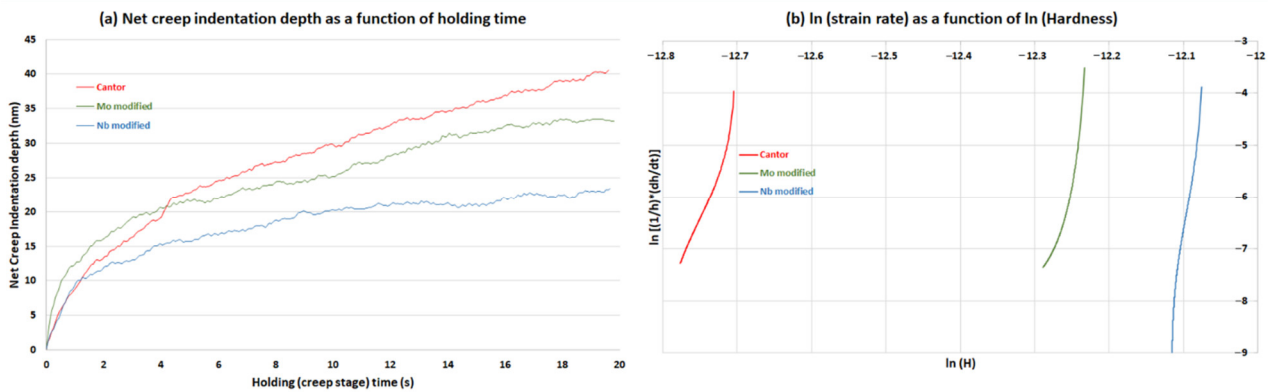

Figure 8. (**a**) Characteristic curves of the net creep indentation depth as a function of time for the different alloy systems. The net Cantor alloy exhibited higher creep depth values, followed by the Mo modified alloy, and the Nb alloy showed the lowest creep indentation depth. (**b**) The characteristic $ln\left(\frac{1}{h}\frac{dh}{dt}\right)$ vs. $ln(H)$ curves of the systems used to calculate the n and m parameters.

Table 4. Stress exponent n actual and extrapolated, strain sensitivity m actual and extrapolated, critical volume for dislocation nucleation, Vcr actual and extrapolated, depth of creep indentation h_{creep}, maximum shear stress τ_{max}.

System	n Extra	n Actual	m Extra	m Actual	V_{cr} Extra (nm³)	V_{cr} Actual (nm³)	h_{creep} (nm)	τ_{max} (GPa)
Cantor	32 ± 8	34 ± 9	0.031 ± 0.008	0.029 ± 0.009	0.196 ± 0.05	0.208 ± 0.06	38 ± 8	0.674 ± 0.05
Mo modified	53 ± 9	63 ± 10	0.019 ± 0.007	0.018 ± 0.007	0.227 ± 0.06	0.269 ± 0.07	33 ± 10	0.960 ± 0.07
Nb modified	107 ± 12	109 ± 12	0.0133 ± 0.009	0.0115 ± 0.09	0.62 ± 0.08	0.414 ± 0.07	23.5 ± 8	1.071 ± 0.09

Based on the data in Table 4, the first point to be mentioned is that, especially from the values of the stress exponent, the creep deformation is mainly dislocation driven, with the power law and power law break down modes to prevail: according to these modes, dislocation slide combined occasionally with dislocation climb are the responsible dislocation movement mechanisms to provide the observed creep deformation [24,26,27,30,61–64]. From the microstructures observed in the previous paragraphs, at least from a statistical point of view, and for the plain Cantor and the Mo modified alloy, the grain boundary sliding and migration phenomena did not contribute to the overall creep deformation [24,26,27,61–65] as the formed grains were very coarse compared to the extent of the indentation depth and trace. This, however, may not be the case in the Nb modified system, as the eutectic microconstituent was of particularly very fine morphology.

It can be observed from the values in Table 4 that the Cantor alloy had the lowest stress exponent values, the highest strain rate sensitivity values, and on the other hand, the Nb modified alloy had the highest stress exponent value, n, and the lower strain rate sensitivity value, m. It has been reported in the literature that high stress exponent values and low strain rate sensitivities correspond to restricted dislocation mobility during creep, lower creep deformation, and higher creep resistance [24,26,27,61–64]. Moreover, in addition to the dislocation mobility, the number of dislocations available for deformation is also very crucial. The critical dislocation nucleation volume is a parameter that depicts this important effect. Clearly, as can be seen in Table 4, the Nb modified system had a higher V_{cr}: this practically means that for the given preset depth, the volume to be activated so that dislocations that will carry potential creep deformation was higher than the other systems (i.e., less dislocations will be generated, less creep deformation is experienced, and higher creep resistance is encountered). These observations are in agreement with similar experimental and research works [24,26,27,61–64]. Moreover, based on the work of Wang et al. [63], it can be seen that the m values obtained in the present effort were quite low, lower than the Al, Mg, and Ti alloys, and even lower than BMGs, a fact that confirmed a high creep resistance. V_{cr} values were also high, indicating a high creep resistance.

3.4. Sliding Wear Response

Figure 9 shows a panoramic view of the alloys' wear track morphologies, produced in the present effort. The monolithic Cantor alloy (Figure 9a) showed the characteristic "hill–valley" morphology, often found in ductile metallic systems [66,67]. This characteristic morphological feature is, very briefly, the result of the extensive plastic deformation of the soft material occurring at the initial stages of the sliding action, which leads to an intensive material movement in front of the steel ball counter— eventually building a "hub" that was characterized as the "hill" area. The process is repeated to the next available area in front of the firstly formed "hill" and eventually the characteristic "hills" separated by "valleys" landscape is formed. For more details of this morphological feature, the reader should address the other works available in the literature [66,67].
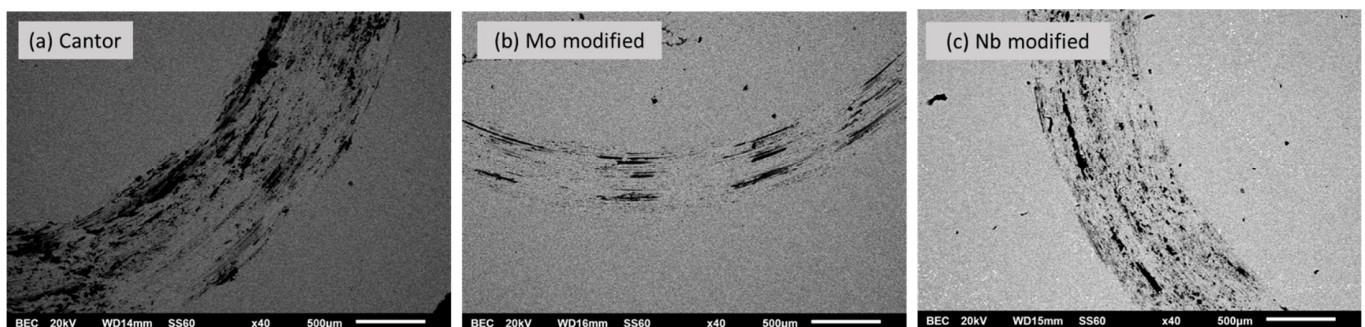

Figure 9. Panoramic view of the alloys' wear track morphologies, produced in the present effort. The characteristic "hill–valley" morphology of the Cantor alloy (**a**) vanished in the other systems (**b,c**).

The modification of the basic Cantor alloy through the introduction of Mo and Nb had a significant effect on the final wear track morphology. Both in the case of the Mo and Nb addition (Figure 9b,c), it could be observed that the "hill–valley" morphology vanished. This elimination suggests the inhibition of extensive plastic deformation and excess material movement, bringing to the front more uniform—throughout the wear tracks—wear mechanisms. Even in the case of Nb, where the wear track size was not severely changed, only a slight reduction in the track width could be observed—the "hill–valley" landscape is vanished. More details on these morphological alterations are presented in the following paragraphs.

Figure 10 shows a comparative indicative diagram of the mass loss as a function of the sliding distance for the three different systems examined in the present effort, which is representative of their behavior during the sliding test experiments. In all cases, an initial stage of extensive mass loss (roughly up to 600 m sliding distance), followed by an almost steady wear mode, was observed. As reported in the literature, this relatively increased mass loss at the initial stage is due to the necessary incubation time required for the elimination/removal of the initial surface asperities [68,69]. After this incubation period, the net wear characteristics can be established (surface oxidation, debris generation, tribolayer formation, etc.) and as such, the steady wear behavior is expressed. From the average values of the slopes for each system after a 600 m sliding distance and the externally applied load (2 N in the present effort), the average wear rate for each alloy (wear rate = slope/external load) was calculated which was found to be 4.0×10^{-6}, 2.25×10^{-6}, and 3.0×10^{-6} g/N.m for the plain Cantor, the modified Mo, and the modified Nb alloys, respectively.
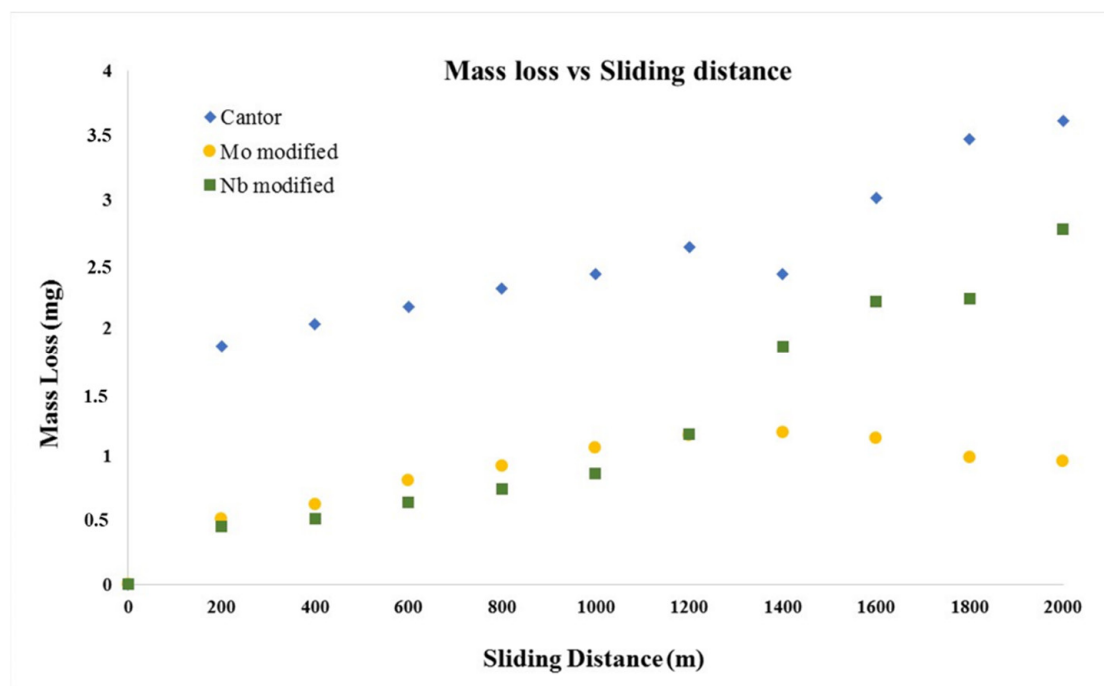

Figure 10. Comparative indicative diagram of mass loss as a function of the sliding distance for the three different systems examined in the present effort.

This tendency is in agreement with both the morphology of the wear tracks presented in Figure 9—the lower the wear rate, the narrower the wear track—and the hardness values presented in the previous paragraphs (i.e., the higher the hardness, the lower the wear rate). This last observation is evidence that the systems obey the classic Archard's law, governing the correlation between hardness and wear rate [70].

Figure 11a–c presents the wear tracks of the different alloys at higher magnification, and the EDS point analysis on the selective areas has also been included for each case. It can be noted that the presence of the oxide phase was evident in their formation to contribute to the overall wear mechanism. What was also observed in Figure 11 is the presence of crack flaws, especially located at the areas of extensive oxidation, which also play an important role in the material loss sequence. Further evidence on the formation of oxide phases can also be found by the EDS analysis on selective areas of the produced upon sliding wear debris. Clearly, as shown in Figure 12a–c, oxide phases were present in all of the different debris formed from the examined systems.

The observations of both the wear tracks and the debris revealed the presence of oxides and flaws/cracks, which directly suggest an oxidative/material detachment wear mode. More specifically, the sequence of deterioration steps can be as follows: (a) Upon the sliding action of the counter-body on the material surface, the temperature due to friction is raised and as the material is exposed to an ambient environment (no specific protective atmosphere was used), surface oxidation takes place, which as the sliding distance increases, becomes more extensive. (b) Within the oxide phase where no plastic deformation can be encountered, the shear action of the counted-body eventually leads to an overcoming of the oxide shear strength and flaws/cracks are formed. Flaw/crack generation can also be supported by potential thermal fatigue phenomena that can be expressed: (a) As the sliding wear test is interrupted every 200 m for specimen weighing, the sample is subjected to a thermal cycle during which the oxide phases cannot (due to lack of plastic deformation) absorb the residual stresses being developed and as such, the formation of crack/flaws can be further enhanced; (b) as the sliding action continues, the cracks/flaws are propagated, enlarged, and finally lead to material removal, revealing a new unexposed material surface, and the circle is repeated. These points suggest an oxidative-detachment wear mechanism. The presence of grooves parallel to the direction of sliding also suggests a partial abrasive wear mode, which was caused by the formation of debris. Similar wear behavior and mechanisms have also been reported in other experimental efforts [50,51,67].
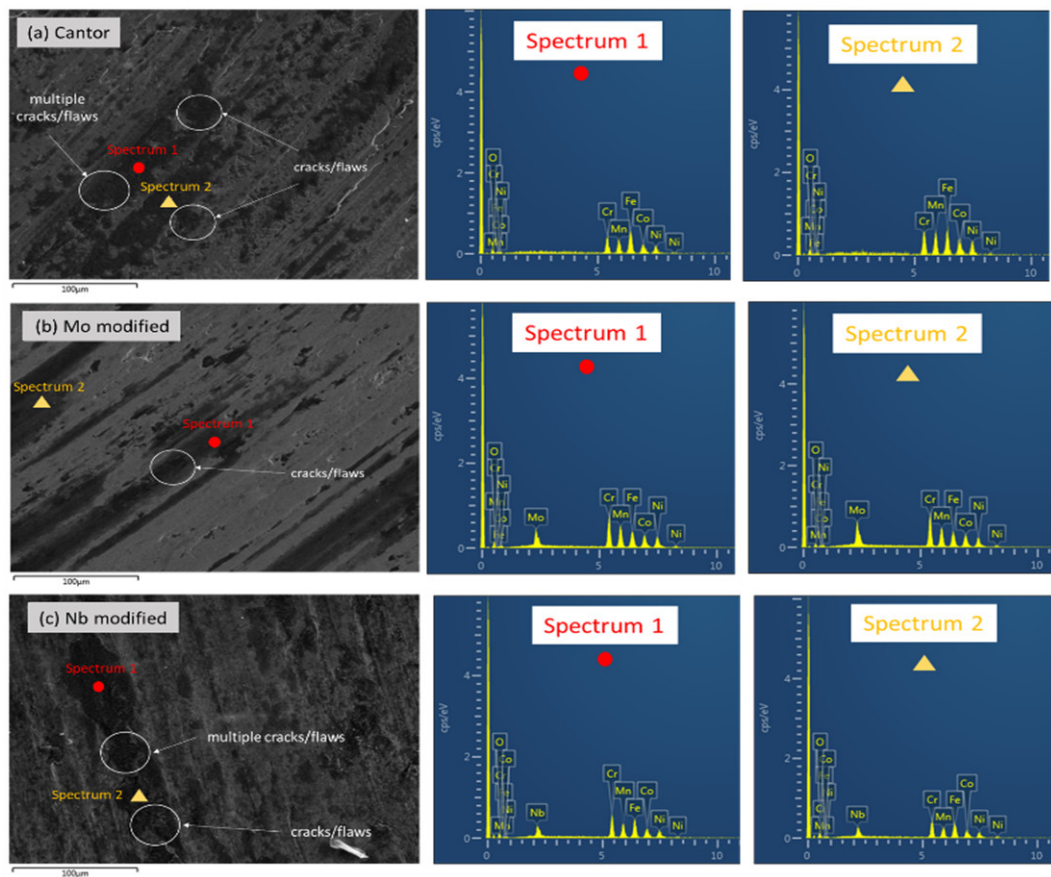

Figure 11. EDS point analysis on selective areas of the wear tracks of (**a**) the plain Cantor alloy; (**b**) the Mo modified system, and (**c**) the Nb modified system. The presence of oxidized areas is evident.
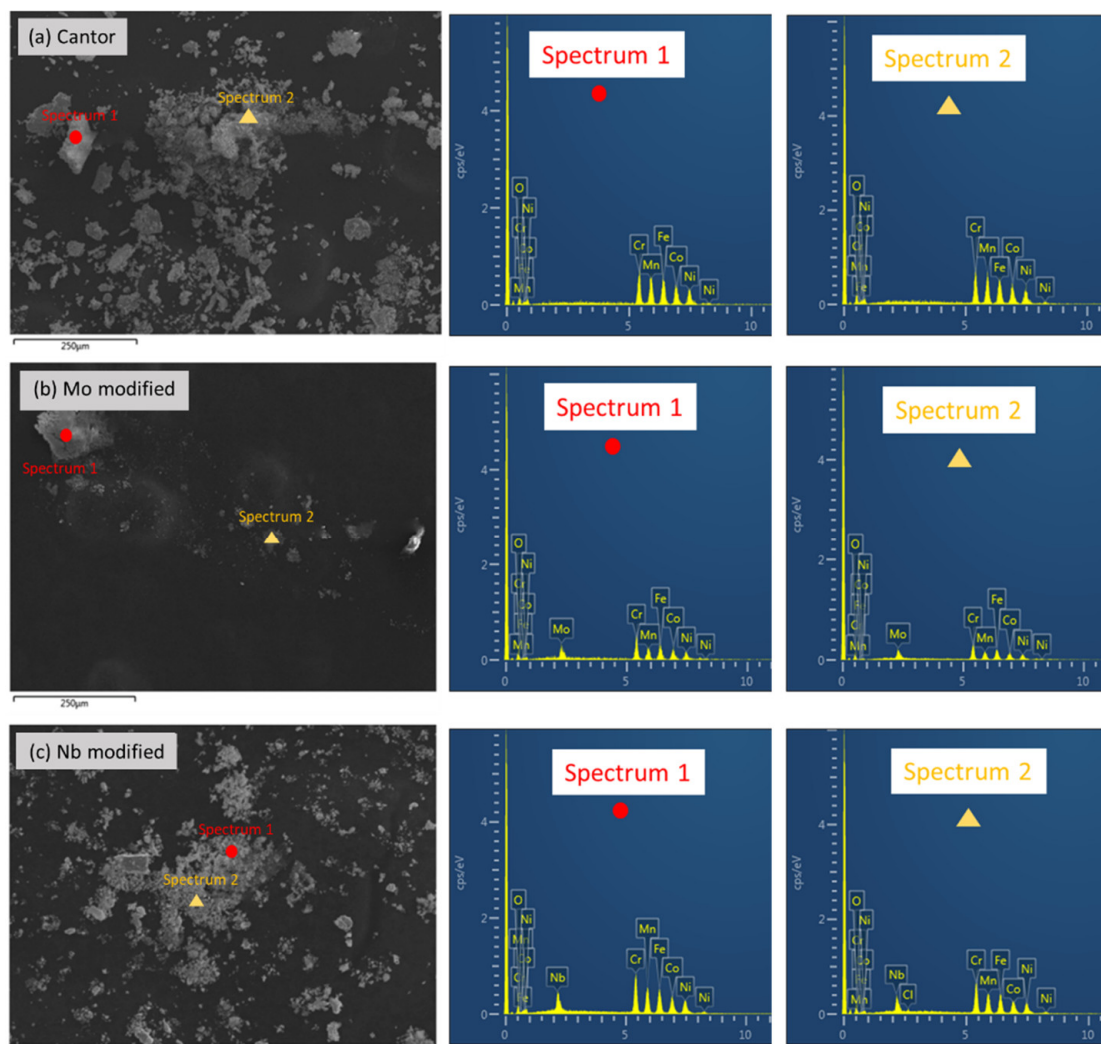
Figure 12. EDS point analysis of the debris for (**a**) the plain Cantor alloy; (**b**) the Mo modified system, and (**c**) the Nb modified system. The presence of oxidized areas is evident.

It is also interesting to correlate the wear track morphology, especially that of the Mo modified system, with the formation of the oxide phase. By recalling the panoramic view shown in Figure 9, it was observed that the wear track of the Mo modified alloy was significantly lower than those of the plain Cantor and the Nb modified system. Mo is considered to be one of the most oxidation resistant elements; moreover, it forms oxide phases with superior lubrication action [71,72]. As such, these combined effects synergistically lead to less material removal (i.e., lower wear rates). Impressively, the reduced material loss was also mirrored in the amount of debris formed in the case of the Mo modified system, as shown in Figure 12b.

4. Conclusions

In this work, Mo and Nb modified Cantor high entropy alloys were studied regarding their microstructural features, mechanical responses, and tribological properties. The XRD analysis of the Cantor alloy verified the simplicity of its microstructure, which consisted of a single FCC phase. The addition of Mo led to phase segregation with new phases such as σ-sigma and BCC being formed. Nb modification resulted in a more complex combination of phases and Laves and possible intermetallics were also identified. The presence of eutectic microconstituents was evident. The parametric model assessment predicted the phase segregation observed in the case of the Mo and Nb modified systems. SEM-EDS analysis verified that the Cantor alloy is a single

FCC phase with uniform element distribution. The Mo modified alloy consisted of a primary BCC phase enriched in Mo, and lastly, a solidified FCC phase was reduced in Mo. The addition of Nb showed that the solidification commenced with a primary rich in Nb phases, which was a combination of BCC and C14 Laves followed by a eutectic microconstituent consisting of C15 Laves and the FCC phase.

Regarding the mechanical response, the introduction of Mo and Nb led to an increase in the indentation modulus of elasticity and hardness due to the presence of new hard phases. The lattice distortion effect due to the presence of the addition of Mo and Nb also contributed to the hardness increase. Creep resistance was observed to increase with the addition of Mo and Nb as the strain exponent increased, the strain rate sensitivity decreased, and most indicatively, the critical volume for dislocation nucleation was increased.

Finally, in terms of sliding wear performance, the wear resistance increased by the modification of Mo and Nb, due to the presence of the new hard phases that were formed and the lubricating action of the multiple oxide phases. Oxidation-delamination wear was the major wear mechanism with some abrasive modes also contributing.

Author Contributions: Conceptulization: E.G. and A.E.K.; Mehtodology: E.G., A.E.K., A.P., A.F., A.S. and S.K.; Investigation: E.G., A.E.K., A.P., A.F., A.S. and S.K.; Data curation: E.G., A.P., S.K. and A.F.; Validation: E.G. and A.E.K.; Writing original draft: A.E.K. and E.G.; Writing review and editing: E.G., A.E.K., A.P., A.F., A.S. and S.K. All authors have read and agreed to the published version of the manuscript.

Institutional Review Board Statement: Not applicable.

Informed Consent Statement: Not applicable.

Data Availability Statement: Not applicable.

Conflicts of Interest: The authors declare no conflict of interest.

References

1. Cantor, B.; Chang, I.T.H.; Knight, P.; Vincent, A.J.B. Microstructural development in equiatomic multicomponent alloys. *Mater. Sci. Eng. A* **2004**, *375*, 213–218. [CrossRef]
2. Yeh, J.W.; Chen, S.K.; Lin, S.J.; Gan, J.Y.; Chin, T.S.; Shun, T.T.; Tsau, C.H.; Chang, S.Y. Nanostructured high-entropy alloys with multiple principal elements: Novel alloy design concepts and outcomes. *Adv. Eng. Mater.* **2004**, *6*, 299–303. [CrossRef]
3. Zhang, Y.; Zuo, T.T.; Tang, Z.; Gao, M.C.; Dahmen, K.A.; Liaw, P.K.; Lu, Z.P. Microstructures and properties of high-entropy alloys. *Prog. Mater. Sci.* **2014**, *61*, 1–93. [CrossRef]
4. Otto, F.; Dlouhý, A.; Pradeep, K.G.; Kuběnová, M.; Raabe, D.; Eggeler, G.; George, E.P. Decomposition of the single-phase high-entropy alloy CrMnFeCoNi after prolonged anneals at intermediate temperatures. *Acta Mater.* **2016**, *112*, 40–52. [CrossRef]
5. Chang, X.; Zeng, M.; Liu, K.; Fu, L. Phase engineering of high-entropy alloys. *Adv. Mater.* **2020**, *32*, 1907226. [CrossRef] [PubMed]
6. Guo, Y.; Su, H.; Zhou, H.; Shen, Z.; Liu, Y.; Zhang, J.; Liu, L.; Fu, H. Unique strength-ductility balance of AlCoCrFeNi$_{2.1}$ eutectic high entropy alloy with ultra-fine duplex microstructure prepared by selective laser melting. *J. Mater. Sci. Technol.* **2022**, *111*, 298–306. [CrossRef]
7. Lu, C.W.; Lu, Y.S.; Lai, Z.H.; Yen, H.W.; Lee, Y.L. Comparative corrosion behavior of Fe$_{50}$Mn$_{30}$Co$_{10}$Cr$_{10}$ dual-phase high-entropy alloy and CoCrFeMnNi high-entropy alloy in 3.5 wt% NaCl solution. *J. Alloys Compd.* **2020**, *842*, 155824. [CrossRef]
8. Cai, Y.P.; Wang, G.J.; Ma, Y.J.; Cao, Z.H.; Meng, X.K. High hardness dual-phase high entropy alloy thin films produced by interface alloying. *Scripta Mater.* **2019**, *162*, 281–285. [CrossRef]
9. Xiao, L.L.; Zheng, Z.Q.; Guo, S.W.; Huang, P.; Wang, F. Ultra-strong nanostructured CrMnFeCoNi high entropy alloys. *Mater. Des.* **2020**, *194*, 108895. [CrossRef]
10. Shahmir, H.; He, J.; Lu, Z.; Kawasaki, M.; Langdon, T.G. Effect of annealing on mechanical properties of a nanocrystalline CoCrFeNiMn high-entropy alloy processed by high-pressure torsion. *Mater. Sci. Eng. A* **2016**, *676*, 294–303. [CrossRef]
11. Schuh, B.; Mendez-Martin, F.; Völker, B.; George, E.P.; Clemens, H.; Pippan, R. Mechanical properties, microstructure and thermal stability of a nanocrystalline CoCrFeMnNi high entropy alloy after severe plastic deformation. *Acta Mater.* **2015**, *96*, 258–268. [CrossRef]

12. Foley, D.L.; Huang, S.H.; Anber, E.; Shanahan, L.; Shen, Y.; Lang, A.C.; Barr, C.M.; Spearot, D.; Lamberson, L.; Taheri, M.L. Simultaneous twinning and microband formation under dynamic compression in a high entropy alloy with a complex energetic landscape. *Acta Mater.* **2020**, *200*, 1–11. [CrossRef]

13. Tsai, S.P.; Tsai, Y.T.; Chen, Y.W.; Chen, P.J.; Chiu, P.H.; Chen, C.Y.; Lee, W.S.; Yeh, J.W.; Yang, J.R. High-entropy CoCrFeMnNi alloy subjected to high-strain-rate compressive deformation. *Mater. Charact.* **2019**, *147*, 193–198. [CrossRef]

14. Otto, F.; Dlouhý, A.; Somsen, C.; Bei, H.; Eggeler, G.; George, E.P. The influences of temperature and microstructure on the tensile properties of a CoCrFeMnNi high-entropy alloy. *Acta Mater.* **2013**, *61*, 5743–5755. [CrossRef]

15. An, X.; Wang, Z.; Ni, S.; Song, M. The tension-compression asymmetry of martensite phase transformation in a metastable $Fe_{40}Co_{20}Cr_{20}Mn_{10}Ni_10$ high-entropy alloy. *Sci. China Mater.* **2020**, *63*, 1797–1807. [CrossRef]

16. Haglund, A.; Koehler, M.; Catoor, D.; George, E.P.; Keppens, V. Polycrystalline elastic moduli of a high-entropy alloy at cryogenic temperatures. *Intermetallics* **2015**, *58*, 62–64. [CrossRef]

17. Zaddach, A.J.; Niu, C.; Koch, C.C.; Irving, D.L. Mechanical properties and stacking fault energies of NiFeCrCoMn high-entropy alloy. *J. Alloys Compd.* **2013**, *65*, 1780–1789. [CrossRef]

18. Tsai, M.T.; Huang, J.C.; Lin, P.H.; Liu, T.Y.; Liao, Y.C.; Jang, J.S.C.; Song, S.X.; Nieh, T.G. Creep of face-centered-cubic {111} and {100} grains in FeCoNiCrMn and FeCoNiCrMn single bond Al alloys: Orientation and solid solution effects. *Intermetallics* **2018**, *103*, 88–96. [CrossRef]

19. Siska, F.; Cech, J.; Hausild, P.; Hadraba, H.; Chlup, Z.; Husak, R.; Stratil, L. Twinning in CoCrFeNiMn high entropy alloy induced by nanoindentation. *Mater. Sci. Eng. A* **2020**, *784*, 139297. [CrossRef]

20. Choi, I.N.; Yoo, B.G.; Kim, Y.J.; Jang, J.I. Indentation creep revisited. *J. Mater. Res.* **2012**, *27*, 3–11. [CrossRef]

21. Bull, S.J. Nanoindentation of coatings. *J. Phys. D Appl. Phys.* **2005**, *38*, 393–413. [CrossRef]

22. Li, W.B.; Henshall, J.L.; Hooper, R.M.; Easterling, K.E. The mechanisms of indentation creep. *Acta Metall. Mater.* **1991**, *39*, 3099–3110. [CrossRef]

23. Ma, Z.S.; Long, S.G.; Zhou, Y.C.; Pan, Y. Indentation scale dependence of tip-in creep behavior in Ni thin films. *Scr. Mater.* **2008**, *59*, 195–198. [CrossRef]

24. Ma, Y.; Feng, Y.H.; Debela, T.T.; Peng, G.L.; Zhang, T.H. Nanoindentation study on the creep characteristics of high-entropy alloy films: Fcc versus bcc structures. *Int. J. Refract. Met. Hard Mater.* **2016**, *54*, 395–400. [CrossRef]

25. Ding, Z.Y.; Song, Y.X.; Ma, Y.; Huang, X.W.; Zhang, T.H. Nanoindentation investigation on the size-dependent creep behavior in a Zr-Cu-Ag-Al bulk metallic glass. *Metals* **2019**, *9*, 613. [CrossRef]

26. Lin, P.H.; Chou, H.S.; Huang, J.C.; Chuang, W.S.; Jang, J.S.C.; Nieh, T.G. Elevated-temperature creep of high entropy alloys via nanoindentation. *MRS Bull.* **2019**, *44*, 860–866. [CrossRef]

27. Zhang, L.; Yu, P.F.; Cheng, H.; Zhang, H.; Diao, H.; Shi, Y.; Chen, B.; Chen, P.; Feng, R.; Bai, J.; et al. Nanoindentation creep behavior of an $Al_{0.3}$CoCrFeNi high-entropy alloy. *Metall. Mater. Trans. A* **2016**, *47*, 5871–5875. [CrossRef]

28. Kang, Y.B.; Shim, S.H.; Lee, K.H.; Hong, S.I. Dislocation creep behavior of CoCrFeMnNi high entropy alloy at intermediate temperatures. *Mater. Res. Lett.* **2018**, *6*, 689–695. [CrossRef]

29. Jiao, Z.M.; Chu, M.Y.; Yang, H.J.; Wang, Z.H.; Qiao, J.W. Nanoindentation characterised plastic deformation of a $Al_{0.5}$CoCrFeNi high entropy alloy. *Mater. Sci. Technol.* **2015**, *31*, 1244–1249. [CrossRef]

30. Wang, Z.; Guo, S.; Wang, Q.; Liu, Z.; Wang, J.; Yang, Y.; Liu, C.T. Nanoindentation characterized initial creep behavior of a high-entropy-based alloy CoFeNi. *Intermetallics* **2014**, *53*, 183–186. [CrossRef]

31. Alhafez, I.A.; Ruestes, C.J.; Bringa, E.M.; Urbassek, H.M. Nanoindentation into a high-entropy alloy-An atomistic study. *J. Alloys Compd.* **2019**, *803*, 618–624. [CrossRef]

32. Wu, D.; Jang, J.S.C.; Nieh, T.G. Elastic and plastic deformations in a high entropy alloy investigated using a nanoindentation method. *Intermetallics* **2016**, *68*, 118–127. [CrossRef]

33. Maier-Kiener, V.; Schuh, B.; George, E.; Clemens, H.; Hohenwarter, A. Insights into the deformation behavior of the CrMnFeCoNi high-entropy alloy revealed by elevated temperature nanoindentation. *J. Mater. Res.* **2017**, *32*, 2658–2667. [CrossRef]

34. Zeng, Z.; Xiang, M.; Zhang, D.; Shi, J.; Wang, W.; Tang, X.; Tang, W.; Wang, Y.; Ma, X.; Chen, Z.; et al. Mechanical properties of Cantor alloys driven by additional elements: A review. *J. Mater. Res. Technol.* **2021**, *15*, 1920–1934. [CrossRef]

35. Kumar, J.; Kumar, N.; Das, S.; Gurao, N.P.; Biswas, K. Effect of Al addition on the microstructural evolution of equiatomic CoCrFeMnNi alloy. *Trans. Indian Inst. Met.* **2018**, *71*, 2749–2758. [CrossRef]

36. Qin, G.; Chen, R.R.; Zheng, H.T.; Fang, H.Z.; Wang, L.; Su, Y.Q.; Guo, J.J.; Fu, H.Z. Strengthening FCC-CoCrFeMnNi high entropy alloys by Mo addition. *J. Mater. Sci. Technol.* **2019**, *35*, 578–583. [CrossRef]

37. Han, Z.D.; Luan, H.W.; Liu, X.; Chen, N.; Li, X.Y.; Shao, Y.; Yao, K.F. Microstructures and mechanical properties of Ti_xNbMoTaW refractory high-entropy alloys. *Mater. Sci. Eng. A* **2018**, *712*, 380–385. [CrossRef]

38. Ma, S.G.; Zhang, Y. Effect of Nb addition on the microstructure and properties of AlCoCrFeNi high-entropy alloy. *Mater. Sci. Eng. A* **2012**, *532*, 480–486. [CrossRef]

39. Zhu, J.M.; Fu, H.M.; Zhang, H.F.; Wang, A.M.; Li, H.; Hu, Z.Q. Synthesis and properties of multiprincipal component $AlCoCrFeNiSi_x$ alloys. *Mater. Sci. Eng. A* **2010**, *527*, 7210–7214. [CrossRef]

40. Li, C.; Li, J.C.; Zhao, M.; Jiang, Q. Effect of aluminum contents on microstructure and properties of Al_xCoCrFeNi alloys. *J. Alloys Compd.* **2010**, *504*, 515–518. [CrossRef]

41. Tong, Y.; Chen, D.; Han, B.; Wang, J.; Feng, R.; Yang, T.; Zhao, C.; Zhao, Y.L.; Guo, W.; Shimizu, Y.; et al. Outstanding tensile properties of a precipitation strengthened FeCoNiCrTi$_{0.2}$ high-entropy alloy at room and cryogenic temperatures. *Acta Mater.* **2019**, *165*, 228–240. [CrossRef]

42. Colombini, E.; Casagrande, A.; Garzoni, A.; Giovanardi, R.; Veronesi, P. Al, Cu and Zr addition to High Entropy Alloys: The effect on recrystallization temperature. *Mater. Sci. Forum* **2018**, *941*, 1137–1142. [CrossRef]

43. Campari, E.G.; Casagrande, A.; Colombini, E.; Gualtieri, M.L.; Veronesi, P. The effect of Zr addition on melting temperature, microstructure, recrystallization and mechanical properties of a Cantor high entropy alloy. *Materials* **2021**, *14*, 5994. [CrossRef] [PubMed]

44. Xu, Z.; Zhang, H.; Li, W.; Mao, A.; Wang, L.; Song, G.; He, Y. Microstructure and nanoindentation creep behavior of CoCrFeMnNi high-entropy alloy fabricated by selective laser melting. *Addit. Manuf.* **2019**, *28*, 766–771. [CrossRef]

45. Findik, F. Latest progress on tribological properties of industrial materials. *Mater. Des.* **2014**, *57*, 218–244. [CrossRef]

46. Joseph, J.; Haghdadi, N.; Shamlaye, K.; Hodgson, P.; Barnett, M.; Fabijanic, D. The sliding wear behaviour of CoCrFeMnNi and Al$_x$CoCrFeNi high entropy alloys at elevated temperatures. *Wear* **2019**, *428*, 32–44. [CrossRef]

47. Shun, T.T.; Chang, L.Y.; Shiu, M.H. Microstructure and mechanical properties of multiprincipal component CoCrFeNiMo$_x$ alloys. *Mater. Char.* **2012**, *70*, 63–67. [CrossRef]

48. He, F.; Wang, Z.; Cheng, P.; Wang, Q.; Li, J.; Dang, Y.; Wang, J.; Liu, C.T. Designing eutectic high entropy alloys of CoCrFeNiNb$_x$. *J. Alloys Compd.* **2016**, *656*, 284–289. [CrossRef]

49. Mathiou, C.; Giorspyros, K.; Georgatis, E.; Poulia, A.; Avgeropoulos, A.; Karantzalis, A.E. NiAl-Cr-Mo-W high-entropy systems: Microstructural verification, solidification considerations and sliding wear response. *Metallog. Microstr. Anal.* **2022**, *11*, 7–20. [CrossRef]

50. Mathiou, C.; Giorspyros, K.; Georgatis, E.; Poulia, A.; Karantzalis, A.E. NiAl-Cr-Mo medium entropy alloys: Microstructural verification, solidification considerations, and sliding wear response. *Materials* **2020**, *13*, 3445. [CrossRef]

51. Mathiou, C.; Giorspyros, K.; Georgatis, E.; Karantzalis, A.E. Microstructural verification of the theoretically predicted morphologies of the NiAl-Cr pseudo-binary alloy systems and NiAl-Cr eutectic structure modification by Mo addition. *SN Appl. Sci.* **2019**, *1*, 1292. [CrossRef]

52. Zhang, Y.; Zhou, Y.J.; Lin, J.P.; Chen, G.L.; Liaw, P.K. Solid solution phase formation rules for multi-component alloys. *Adv. Eng. Mater.* **2008**, *10*, 534–538. [CrossRef]

53. Wang, Z.; Huang, Y.; Yang, Y.; Wang, J.; Liu, C.T. Atomic-size effect and solid solubility of multicomponent alloys. *Scr. Mater.* **2015**, *94*, 28–31. [CrossRef]

54. Guo, S.; Ng, C.; Lu, J.; Liu, C.T. Effect of valence electron concentration on stability of fcc or bcc phase in high entropy alloys. *J. Appl. Phys.* **2011**, *109*, 103505. [CrossRef]

55. Yang, X.; Zhang, Y. Prediction of high-entropy stabilized solid-solution in multi-component alloys. *Mater. Chem. Phys.* **2012**, *132*, 233–238. [CrossRef]

56. Senkov, O.N.; Miracle, D.B. A new thermodynamic parameter to predict formation of solid solution or intermetallic phases in high entropy alloys. *J. Alloys Compd.* **2016**, *658*, 603–607. [CrossRef]

57. Troparevsky, M.C.; Morris, J.R.; Kent, P.R.C.; Lupini, A.R.; Stocks, G.G. Criteria for predicting the formation of single-phase high-entropy alloys. *Phys. Rev. X* **2015**, *5*, 011041. [CrossRef]

58. Phase Diagram. Available online: https://sites.google.com/site/catcalcphase/metal/cr/cr-nb (accessed on 15 April 2022).

59. Oliver, W.C.; Pharr, G.M. Measurement of hardness and elastic modulus by instrumented indentation: Advances in understanding and refinements to methodology. *J. Mater. Res.* **2004**, *19*, 3–20. [CrossRef]

60. Milman, Y.V.; Golubenko, A.A.; Dub, S.N. Indentation size effect in nanohardness. *Acta Mater.* **2011**, *59*, 7480–7487. [CrossRef]

61. Karantzalis, A.E.; Mathiou, C.; Kyrtsidou, K.; Georgatis, E. Primary nano-indentation assessment of low entropy NiAl-Cr alloys. *SOJ Mater. Sci. Eng.* **2022**, *10*, 1–15.

62. Karantzalis, A.E.; Sioulas, D.; Poulia, A.; Mathiou, C.; Georgatis, E. A first approach on the assessment of the creep behavior of MoTaNbV$_x$Ti high entropy alloys by indentation testing. *SN Appl. Sci.* **2020**, *2*, 950. [CrossRef]

63. Wang, D.; Tan, J.; Li, C.J.; Qin, X.M.; Guo, S.F. Enhanced creep resistance of Ti$_{30}$Al$_{25}$Zr$_{25}$Nb$_{20}$ high-entropy alloy at room temperature. *J. Alloys Compd.* **2021**, *885*, 161038. [CrossRef]

64. Yu, P.F.; Feng, S.D.; Xu, G.S.; Guo, X.L.; Wang, Y.Y.; Zhao, W.; Qi, L.; Li, G.; Liaw, P.K.; Liu, R.P. Room-temperature creep resistance of Co-based metallic glasses. *Scr. Mater.* **2014**, *90*, 45–48. [CrossRef]

65. Hu, J.D.; Xuan, F.Z.; Liu, C.J.; Chen, B. Modelling of cavity nucleation under creep-fatigue interaction. *Mech. Mater.* **2021**, *156*, 103799. [CrossRef]

66. Sarkar, A.D. *Friction and Wear*; Academic Press: London, UK, 1980; pp. 205–209.

67. Mavros, H.; Karantzalis, A.E.; Lekatou, A. Solidification observations and sliding wear behavior of cast TiC particulate-reinforced AlMgSi matrix composites. *J. Compos. Mater.* **2012**, *47*, 2149–2162. [CrossRef]

68. Suh, N.P. The delamination theory of wear. *Wear* **1973**, *25*, 111–124. [CrossRef]

69. Suh, N.P. An overview of the delamination theory of wear. *Wear* **1977**, *44*, 1–16. [CrossRef]

70. Archard, J.F.; Hirst, W. The wear of metals under unlubricated conditions. *Proc. R. Soc. Lond. A* **1956**, *236*, 397–410.

71. Glascott, J.; Stott, F.H.; Wood, G.C. The effectiveness of oxides in reducing sliding wear of alloys. *Oxid. Met.* **1985**, *24*, 99–114. [CrossRef]

72. Stott, F.H.; Wood, G.C. The influence of oxides on the friction and wear of alloys. *Tribol. Int.* **1978**, *11*, 211–218. [CrossRef]